

OPEN ACCESS

A Comparative Study on the Activity and Stability of Iridium-Based Co-Catalysts for Cell Reversal Tolerant PEMFC Anodes

To cite this article: Robert Marić *et al* 2023 *J. Electrochem. Soc.* **170** 084505

View the [article online](#) for updates and enhancements.

You may also like

- [Study the properties of activated carbon and oxyhydroxide aluminum as sorbents for removal humic substances from natural waters](#)
L N Shiyani, K I Machekhina and E N Gryaznova
- [Transformation of the OER-Active IrO_x Species under Transient Operation Conditions in PEM Water Electrolysis](#)
Philipp Jan Rheinländer and Julien Durst
- [Recent progress in *in situ/operando* analysis tools for oxygen electrocatalysis](#)
Ji Mun Yoo, Heejong Shin, Subin Park et al.



Your Lab in a Box!

The PAT-Tester-i-16: All you need for Battery Material Testing.

- ✓ All-in-One Solution with integrated Temperature Chamber!
- ✓ Cableless Connection for Battery Test Cells!
- ✓ Fully featured Multichannel Potentiostat / Galvanostat / EIS!

www.el-cell.com +49 40 79012-734 sales@el-cell.com

EL-CELL[®]
electrochemical test equipment





A Comparative Study on the Activity and Stability of Iridium-Based Co-Catalysts for Cell Reversal Tolerant PEMFC Anodes

Robert Marić,^{1,2,*} Christian Gebauer,¹ Florian Eweiner,¹ and Peter Strasser^{2,*,*,z}

¹Hydrogen Systems, Heraeus Deutschland GmbH & Co. KG, Hanau 63450, Germany

²Electrochemical Catalysis, Energy, and Materials Science Laboratory, Technische Universität Berlin, Berlin 10623, Germany

In fuel cell applications with long lifetime requirements, the management of stressing operating conditions—such as hydrogen starvation events—plays a pivotal role. Among other remedies, the incorporation of an OER-enhancing co-catalyst, is widely employed to improve the intrinsic stability of Pt/C-based anode catalyst layers in PEM fuel cells. The present study investigates several supported and unsupported Ir-based co-catalysts comprising different oxidation states of iridium: from metallic to oxidic character, both anhydrous rutile-type IrO₂ and hydrated amorphous form. Utilizing a single-cell setup, cell reversal experiments were conducted initially after break-in of the MEA and after seven days of continuous operation under reductive H₂ atmosphere at application-relevant conditions. The initial cell reversal tolerance was found to increase in the order metallic Ir < crystalline Ir oxide < amorphous Ir oxyhydroxide. By contrast, after continuous operation under H₂ the order changes drastically to amorphous Ir oxyhydroxide ~ metallic Ir < crystalline Ir oxide. This led us to conclude that the amorphous Ir oxyhydroxide is likely reduced to metallic Ir during continuous H₂ operation, while IrO₂ provides a reasonable trade-off between initial OER activity, high structural and chemical stability at high anode potentials during H₂ starvation and low reducibility under prolonged H₂ operation. © 2023 The Author(s). Published on behalf of The Electrochemical Society by IOP Publishing Limited. This is an open access article distributed under the terms of the Creative Commons Attribution Non-Commercial No Derivatives 4.0 License (CC BY-NC-ND, <http://creativecommons.org/licenses/by-nc-nd/4.0/>), which permits non-commercial reuse, distribution, and reproduction in any medium, provided the original work is not changed in any way and is properly cited. For permission for commercial reuse, please email: permissions@iopublishing.org. [DOI: 10.1149/1945-7111/aceb8d]



Manuscript submitted February 24, 2023; revised manuscript received June 19, 2023. Published August 9, 2023.

Supplementary material for this article is available [online](#)

In view of the upcoming use of proton exchange membrane fuel cells (PEMFC) in applications with high lifetime requirements such as heavy-duty vehicles, the management of difficult operating conditions is of key importance.¹ Besides numerous efforts to tailor the stability of the cathode catalyst to meet these requirements,^{2–4} special emphasis has been placed on cell reversal events triggered by hydrogen starvation, which cause a sharp decline in performance within seconds due to extensive corrosion of the carbon-supported Pt catalyst at the anode catalyst layer. Among other remedies,^{5–12} the incorporation of a second catalyst component that favors the harmless oxygen evolution reaction (OER) over the destructive carbon oxidation reaction (COR) is a widespread strategy to improve the intrinsic stability of the anode catalyst layer during fuel starvation.^{10,13–17} From research and development on PEM water electrolysis (PEMWE), iridium-based catalysts emerged as particularly active towards the OER^{18–24} and are therefore promising co-catalysts in PEMFC anode electrodes to enhance the cell reversal tolerance. The limited iridium availability of approx. 10 metric tons per year²⁵ and the competing demand with current and emerging applications, such as PEMWE, calls for material innovation to tackle lifetime limiting stress events in PEMFC anodes with a sustainable use of iridium as an OER enhancing co-catalyst.

The OER activity and stability of precious metals-based catalysts has been extensively studied in both metallic^{26–28} and oxide forms.^{27,29–32} In terms of stability, particular emphasis has been placed on high potential and transient potential experiments in half-cell configuration to study the dissolution stability of the OER catalysts, combined with in-line inductively coupled plasma mass spectrometry (ICP-MS) to determine the dissolved metal concentration in the electrolyte^{27,33} or electrochemical quartz crystal microbalance (EQCM) technique to track potential induced mass changes.³⁴ It was reported that the dissolution rate for metallic iridium is about two orders of magnitude higher than for iridium oxide in acidic media,^{27,35} the latter being usually divided into two categories, namely highly defective amorphous and anhydrous

crystalline iridium oxide. In this context, heat treatment of (partially) amorphous iridium oxide catalysts has been used to produce more crystalline and durable catalysts,^{21,32,35,36} albeit accompanied with lower activity.

In view of the application of the OER catalysts in PEMFC anodes, a vast majority of literature deals with the investigation of the efficacy of the developed cell reversal tolerant anodes immediately after fabrication and short break-in of the membrane electrode assemblies (MEA).^{14,16,37–40} Only few studies^{33,41–43} focused on the correlation of the dissolution stability of Ir-based OER co-catalysts during transient voltage operation, which would occur at the anode side during start-up/shut-down events (reverse-current mechanism⁴⁴) or during pulsed cell reversal events,⁴⁵ and investigated its potential impact on cell reversal tolerance. It has been proposed that soluble Irⁿ⁺ species^{30,46,47} form as an intermediate between metallic Ir and IrO₂ during voltage cycling that migrate through the ionic phase to the cathode, thereby degrading the cell reversal tolerance and cathode catalyst activity. However, there is little understanding on the stability of the OER co-catalysts under reductive, meaning normal operating conditions (pH ≤ 1 and approx. 0 V) in presence of an H₂ atmosphere at elevated temperatures^{41,42} and how this in turn affects the cell reversal tolerance on MEA level. Moreover, to the best of our knowledge, we are not aware of a comprehensive cell reversal study that systematically examines iridium-based co-catalysts with various chemical oxidation states, i.e. metallic and oxidic character, both anhydrous rutile-type IrO₂ and hydrated amorphous form in in-situ MEA experiments.

In this study, we investigate five different OER co-catalysts for PEMFC anodes, namely unsupported Ir-black and IrO₂, their carbon-supported variants metallic iridium (Ir/C) and crystalline iridium oxide (IrO₂/C), as well as an amorphous iridium oxyhydroxide (a-IrO_x(OH)_y/C). The cell reversal tolerance is determined both initially after break-in of the MEAs and in a second dedicated experiment after prolonged (seven days) of continuous cell operation in H₂/Air. In contrast to previous studies, in the latter experiment the OER co-catalysts are permanently exposed to a reducing atmosphere instead of being subjected to transient voltage conditions. The studies of the MEAs are complemented by basic electrochemical analysis of the OER co-catalysts in the rotating disk electrode (RDE) and X-ray photoelectron spectroscopy (XPS). The results indicate

*Electrochemical Society Student Member.

**Electrochemical Society Member.

^zE-mail: pstrasser@tu-berlin.de

that the initial reversal tolerance of the MEAs decreases to different degrees after continuous operation in reductive atmosphere depending on the iridium species present. Notably, highly active amorphous iridium oxyhydroxide is presumably reduced to less active metallic iridium during H₂ operation and loses its initial highly stabilizing effect, while IrO₂ provides a reasonable trade-off between initial OER activity and reduction stability.

Experimental

Catalysts and MEA components.—Five types of MEAs with an active area of 50 cm² were prepared, differing in the employed OER co-catalyst (*I-V*) on the anode. For all samples, the anode comprised 30 wt.% platinum on a highly graphitized low surface area (LSA; H2FC-30PtC60T, Heraeus Deutschland GmbH & Co. KG) carbon support, while the cathode contained 40 wt.% platinum on a commercially available medium surface area (MSA) carbon support (Vulcan XC72R, Cabot Corporation). The final platinum catalyst layer loading was 0.1/0.4 mg_{Pt} cm⁻²_{geo} for the anode and cathode, respectively. Additionally, one of the synthesized iridium-based catalysts listed below was added to the anode catalyst layer with an iridium metal content of 15 wt.% relating to the platinum loading of the catalyst layer, i.e. 15 μg_{Ir} cm⁻²_{geo}. To improve the cell reversal stability, either (*I*) unsupported metallic iridium, hereinafter referred as Ir-black, (*II*) rutile-type IrO₂ (H2EL-IrO, Heraeus Deutschland GmbH & Co. KG), (*III*) carbon-supported metallic iridium, 30 wt.% Ir/C, (*IV*) carbon-supported crystalline iridium oxide, 30 wt.% IrO₂/C, or (*V*) carbon-supported amorphous iridium oxyhydroxide, 30 wt.% a-IrO_x(OH)_y/C was applied. Notably, the same LSA carbon as mentioned above was used as carrier for the supported iridium catalysts, which were prepared by a confidential synthesis method by Heraeus. As described in a previous publication,⁴⁵ anode and cathode catalyst layers were fabricated with an I/C ratio ($\frac{g_{\text{ionomer}}}{g_{\text{carbon}}}$) of 1.0 (20 wt.% NafionTM D2020, 46 wt.% isopropanol, 34 wt.% water, The Chemours Company), hot-pressed onto a commercial membrane (Gore M820.15, W. L. Gore & Associates, Inc.), sandwiched between two gas diffusion layers (GDL, Sigracet 28BC, SGL Carbon GmbH) with a compression of about 20% adjusted by using glass fiber reinforced PTFE gaskets (Fiberflon GmbH) to form the final MEA with an active area of 50 cm².

OER co-catalyst characterization.—The OER co-catalyst powders were initially characterized in terms of their electrochemical and physico-chemical properties. RDE was used to obtain cyclic voltammograms (CV) and the activity towards the OER. The measurement was conducted in a three-electrode setup using a calomel reference electrode (Hg/Hg₂Cl₂, 3 mol l⁻¹ KCl), a Pt foil counter electrode, and a glassy carbon disk (0.196 cm²) working electrode embedded in a PEEK shroud in a jacketed glass cell (Pine Research Instrumentation) in 0.5 M sulfuric acid (suprapur sulphuric acid ≥ 96%, Merck, diluted using ultra-pure water, 18 MΩ cm⁻¹, Milli-Q[®]) as liquid electrolyte. The working electrodes were prepared by mixing the respective OER catalyst with a PFSA dispersion (20 wt.% NafionTM D2020, 46 wt.% isopropanol, 34 wt.% water, The Chemours Company) and ultra-pure water (18 MΩ cm⁻¹, Milli-Q[®]). The ionomer to catalyst ratio is calculated to be 0.116. The catalyst containing ink (2 mg_{cat} ml⁻¹_{ink}) was subsequently homogenized in an ultrasonic bath. Thereafter the 9.8 μl ink was pipetted onto the RDE tip and dried overnight. The catalyst loading on the RDE tip was calculated to be 100 μg_{cat} cm⁻². After saturating the liquid electrolyte with N₂ (N5.0), six CVs were measured between 0–1.00 V_{RHE} at a scan rate of 100 mV s⁻¹ at 60 °C. The data shown within this work are based on the sixth scan. Note that the applied potential was corrected against the reversible hydrogen electrode by approx. 234 mV (reference electrode was calibrated using Pt foil as working and counter electrode in the same H₂-saturated electrolyte at 60 °C at 1 mV s⁻¹ scan rate, correction towards RHE taking the elevated temperature into account). The OER activity was determined by recording a CV at a scan rate of

10 mV s⁻¹ between 1.00–1.55 V_{RHE} in air saturated electrolyte applying a rotation rate of 1600 rpm. The mass activity was taken at 1.50 V_{RHE} based on the cathodic scan.

XPS—as a surface sensitive technique—is applied to quantitatively analyze the chemical state of the Ir-based OER catalysts. The powder samples were placed on a stainless-steel holder. The measurement is performed using a PHI 5800 ECSA system (Physical Electronics, Inc.) in ultra-high vacuum with a background pressure of 5·10⁻⁹ mbar and a Mg Kα X-ray source at a power of 400 W. While the overview spectra were obtained with a pass energy of 117 eV, the detailed spectra (Ir 4f, O 1s) were measured with 23.5 eV pass energy which yield an approximate energy resolution of 0.5 eV for the Ir 4f line. The binding energy was calibrated by measuring Au 4f_{7/2} (83.95 eV) on an inserted specimen. The core level spectra were fitted using the commercially available CasaXPS software after subtraction of a Shirley-type background. The doublet peak separation and peak area ratio of Ir 4f_{7/2} and Ir 4f_{5/2} were constrained to 2.98 eV and 4:3, respectively. As recommended for conductive samples,⁴⁸ fitting is achieved using a line shape appropriate for asymmetric peak shapes, i.e. Functional Lorentzian (LF). Details on the fitting parameters can be found in Tab. S1.

MEA characterization.—On MEA level, the electrochemical studies were performed on a G40 test bench (Greenlight Innovation Corp.) in single-cell configuration using a multichannel serpentine graphite flow field in counter-flow mode. Prior to the actual cell reversal experiments, all MEAs were conditioned and initially characterized in polarization curves as described elsewhere.⁴⁵ Briefly, eight consecutive break-in cycles were applied, comprising the following potentiostatic partial steps—(i) 0.6 V for 45 min, (ii) 0.95 V for 5 min, and (iii) 0.85 V for 10 min—at 60 °C cell and dew point temperatures (i.e. relative humidity, RH = 100%), symmetrical pressure of 150 kPa_{abs,inlet}, flow rates of 1400/3300 nccm in H₂ (N6.0)/Air (N5.0). Subsequently, the beginning-of-life (BOL) performance was obtained at 80 °C cell and dew point temperatures in fully humidified H₂/Air (RH = 100%), constant flow rates of 1000/5000 nccm and symmetrical pressures of 150 kPa_{abs,inlet} at both electrodes.

The hydrogen starvation tests were split into two independent approaches (A) and (B), the first to determine the cell reversal tolerance immediately after initial conditioning and performance characterization, the latter to assess the cell reversal tolerance after seven days of continuous operation under reductive hydrogen conditions. (A) One full set of MEAs—differing in the OER co-catalyst applied—were immediately exposed to cell reversal experiment. The measurement was performed at 80 °C cell and dew point temperatures (RH = 100%), 150 kPa_{abs,inlet} symmetrical pressures and 1000/5000 nccm flow rates. A constant load of 0.2 A cm⁻²_{geo} was externally supplied throughout the experiment utilizing a 3 A potentiostat (Reference 3000, Gamry Instruments, Inc.) extended with a 30 A booster (Reference 30k Booster, Gamry Instruments, Inc.). The MEAs were operated in H₂/Air for 10 min, then the anode gas was switched to fully humidified N₂ (N5.0) which triggered the hydrogen starvation event. The occurrence of cell reversal is indicated by a sharp drop in cell voltage below 0 V within a few seconds. The time a MEA can withstand these conditions until it reaches a given cut-off voltage (–1.25 V for our study), is used as a measure of cell reversal tolerance.^{10,15,16,49–52} Finally, the end-of-life (EOL) performance was determined following the conditions of the BOL performance measurement. (B) Another set of MEAs was first subjected to periodically altered conditions for seven consecutive days, consisting of 22 h constant operation at 0.65 V in H₂/Air, followed by an intermittent polarization curve (approx. 2 h) under the same temperatures, pressures and flow rates as described for the BOL polarization curve. Afterwards, the above-described cell reversal experiment was applied, and the EOL polarization curve was examined. The results of the polarization curve measurements are summarized in the supplementary information in Fig. S1.

CO-stripping voltammograms were performed for selected samples (Pt/C only and a- $\text{IrO}_x(\text{OH})_y/\text{C}$ containing MEAs) immediately after break-in and after prolonged operation under H_2 for seven consecutive days before conducting any cell reversal experiment. The operating conditions were set to 35 °C, 100% RH and ambient pressures symmetrically applied for both electrodes, with the anode side flushed with 50 nccm N_2 (N5.0) connected as working electrode and the cathode side flushed with 500 nccm 5% H_2 (balance sat. N_2 N5.0) connected as counter/reference electrode. Ten cleaning CVs were recorded in the voltage range of 0.07–1.0 V_{RHE} with a scan rate of 100 mV s^{-1} utilizing the above-described potentiostat/booster combination. For CO-stripping experiment, a cell voltage of 0.1 V was held for 30 min while feeding the anode successively with 100 nccm 5% CO in N_2 (N5.0) for 5 min, followed by 50 nccm N_2 for 20 min to remove residue CO and 50 nccm N_2 for 5 min. During CO purging, the gas was routed through a dry bypass to limit contamination of the humidifier. Three CVs were subsequently recorded at a scan rate of 20 mV s^{-1} between 0.1–1.05 V_{RHE} .

Results and Discussion

In first instance, to gather insights into the surface chemistry of the Ir-based OER catalysts, cyclic voltammograms (CVs) were recorded utilizing a rotating disk electrode (RDE). Figure 1a depicts the CVs of the unsupported bulk catalysts, where Ir-black (black) features the typical underpotential hydrogen desorption/adsorption (upd) peaks between 0.1–0.3 V_{RHE} and Ir surface oxidation/reduction peaks in the range of 0.4–1.0 V_{RHE} , while the rutile-type IrO_2 (blue) shows only minor redox features, as previously found elsewhere.^{20,21} In Fig. 1b the supported OER catalysts are shown, metallic Ir on a low surface area (LSA) carbon carrier (Ir/C, gray), crystalline iridium oxide (IrO_2/C , light blue) and an amorphous iridium oxyhydroxide (a- $\text{IrO}_x(\text{OH})_y/\text{C}$, red). While Ir/C and IrO_2/C exhibit similar characteristics to their unsupported variants—Ir-black and IrO_2 respectively—the a- $\text{IrO}_x(\text{OH})_y/\text{C}$ shows distinct redox features above 0.3 V_{RHE} that can be assigned to the transitions between Ir^{III} and Ir^{IV} , and vice versa, while hydrogen desorption/adsorption peaks are absent in the low voltage regime,⁵³ which indicates a vanishing catalyst film conductivity at low potentials. Accordingly, similar prevailing features in the cyclic voltammograms confirm the successful synthesis of OER co-catalysts with similar chemical states with the following groupings: Ir-Black and supported Ir/C; IrO_2 and supported IrO_2/C ; supported a- $\text{IrO}_x(\text{OH})_y/\text{C}$.

The qualitative observations of the electrochemical measurement were complemented by quantitative analysis of the prevalent chemical state of the catalyst powders by X-ray photoelectron spectroscopy. Table S1 summarizes the applied fitting parameters as well as the obtained peak position, full width at half maximum (FWHM) and the calculated composition of the Ir 4f core level spectra of each OER catalyst. Figure 2 illustrates the measured XPS Ir 4f spectra (black dotted line), the fitted chemical states— Ir^0 (black shaded region), Ir^{III} (red shaded region), Ir^{IV} (blue shaded region)—and the resulting fit envelope (green line). From Figs. 2a and 2b, the metallic character of both Ir-black and Ir/C is evident, with the main Ir^0 4f_{7/2} peak position at a binding energy of 60.8–60.9 eV, which is in good agreement with other findings.^{42,48,54,55} On the other hand, the shapes of the XPS spectra in Figs. 2c and 2d, elucidate the similar chemical oxidation state of the IrO_2 and IrO_2/C catalysts, which primarily comprises Ir^{IV} (>85 at.%) with small amounts of Ir^{III} . In contrast, the a- $\text{IrO}_x(\text{OH})_y/\text{C}$ in Fig. 2e consists mainly of Ir^{III} (~70 at.%) with minor Ir^{IV} shares. According to the applied line shapes, the main peak positions of the respective Ir^{IV} and Ir^{III} 4f_{7/2} main peaks are located at a binding energy of 61.5–61.6 eV and 62.0–62.4 eV, coinciding well with other studies.^{42,54} Note that although the existence of satellite peaks has been predicted by calculations and partially fitted in the scientific literature,⁵⁴ their use was omitted within this work due to less resolved XPS spectra. Instead, a Functional Lorentzian (LF) asymmetric line shape was used to account for the conductive samples⁴⁸ as well as satellites,

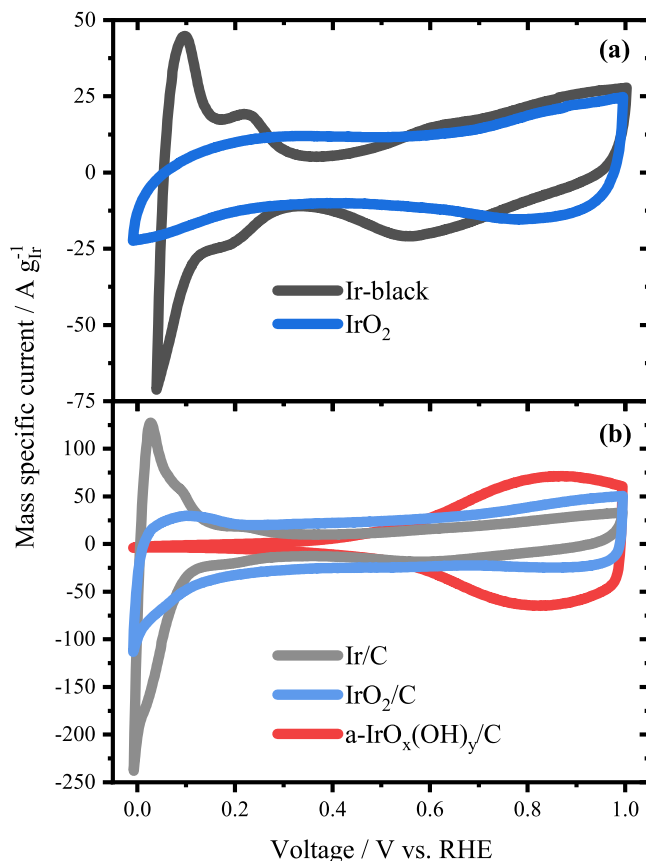


Figure 1. Cyclic voltammograms (CVs) of the oxygen evolution (OER) co-catalysts, (a) unsupported Ir-black (black line), and IrO_2 (dark blue line), (b) carbon-supported metallic iridium 30 wt.% Ir/C (grey line), carbon-supported crystalline iridium oxide 30 wt.% IrO_2/C (light blue line), and carbon-supported amorphous iridium oxyhydroxide 30 wt.% a- $\text{IrO}_x(\text{OH})_y/\text{C}$ (red line). CVs: RDE, 100 mV s^{-1} , 60 °C, N_2 sat. 0.5 M H_2SO_4 .

which at least allows to identify the predominant iridium oxidation state without claiming absolute accuracy in the analyzed composition. However, the consistency between the RDE and XPS results confirms the robustness of the conclusions drawn about the prevailing chemical state of the catalysts. The O 1s spectra of the oxidic catalysts in Fig. 3 further confirm the similar structure between IrO_2 and IrO_2/C ,⁵⁶ while a shift of ~0.9 eV in the binding energy of the peak maxima indicates more hydroxyl character⁴⁸ for the a- $\text{IrO}_x(\text{OH})_y/\text{C}$, again confirming the initial dominant Ir^{III} state, whose further oxidation was strongly pronounced in the respective CV (cf. Fig. 1b).^{57,58} Notably, a detailed fit of the O 1s spectra was not performed due to inaccuracies associated with additional O 1s peaks due to oxygen functional groups on the carbon support.

Based on the insights into the chemical state, the activities towards the oxygen evolution reaction of the different co-catalysts were evaluated and ranked. Figure 4 presents a bar chart with the mass activities derived from the RDE measurements at 60 °C in acidic electrolyte. With respect to the different iridium catalysts, the mass activity increases from 90 to approx. 750 $\text{A g}^{-1}_{\text{Ir}}$ at 1.5 V_{RHE} in the following order: $\text{IrO}_2 < \text{Ir-black} \ll \text{IrO}_2/\text{C} < \text{Ir/C} \ll \text{a-IrO}_x(\text{OH})_y/\text{C}$. Supported by a number of comparative studies, the subsequent relative trends are derived with respect to the chemical and structural properties of the catalyst employed: (1) metallic iridium is more active in catalyzing the OER than its rutile-type oxide,^{27,59} (2) supported nanoparticles exhibit higher OER activity compared to their corresponding bulk catalysts,^{60–63} (3) amorphous iridium oxyhydroxide structures are more active than their crystalline counterparts.^{21,64,65}

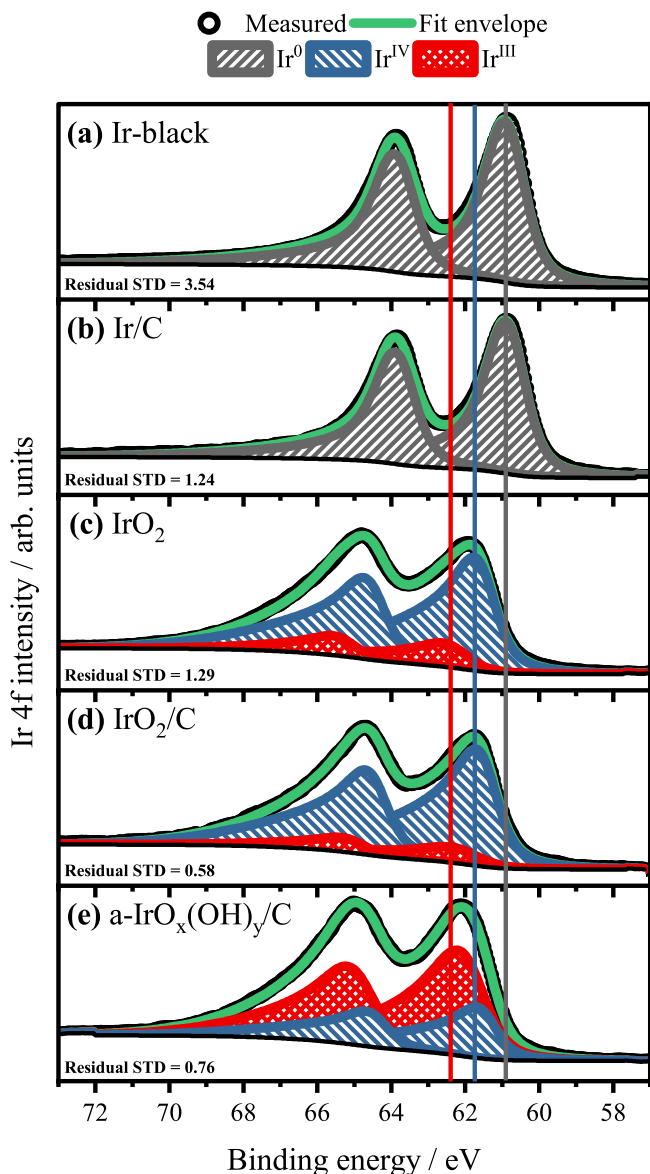


Figure 2. XPS Ir 4f with core spectra (black circles), fitted chemical states— Ir^0 (grey shaded region), Ir^{III} (red shaded region), Ir^{IV} (blue shaded region)—and the resulting fit envelope (green line) of (a) unsupported Ir-black, (b) carbon-supported metallic iridium 30 wt.% Ir/C, (c) IrO_2 , (d) carbon-supported crystalline iridium oxide 30 wt.% IrO_2/C , and (e) carbon-supported amorphous iridium oxyhydroxide 30 wt.% $\text{a-IrO}_x(\text{OH})_y/\text{C}$. Colored vertical lines represent the binding energy position of the main Ir 4f peaks of Ir^0 , Ir^{III} and Ir^{IV} .

In this context, the origin of the high OER activity of Ir-based catalysts along with a detailed explanation of the chemical/electronic structure of the active species has been a major research objective in past decades. Early studies indicated that electrochemical cycling of metallic iridium within a certain potential range causes an oxide/hydroxide transition which enhances the OER activity.^{47,66} Later reports on high surface area iridium oxide showed that amorphous forms exhibit higher OER activity than crystalline counterparts.^{21,67,68} In this regard, correlations between heat-treatment temperature and loss of activity of those catalysts were revealed and attributed to the formation of crystalline rutile-type IrO_2 at elevated temperatures.^{21,32,35,53,69,70} Recent efforts to characterize and model the electronic structure of Ir-based catalysts have aimed to uncover the molecular mechanisms behind the high OER activity. The authors suggest that the presence of OER-relevant electrophilic $\text{O}^{\text{I-}}$ in Ir^{III} -rich oxyhydroxides facilitates the O-O bond formation during the OER by

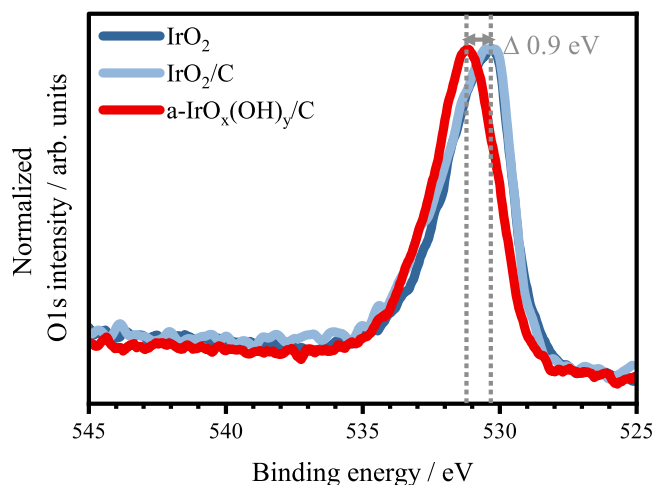


Figure 3. Normalized XPS O 1s core spectra of unsupported IrO_2 (dark blue line), carbon-supported crystalline iridium oxide 30 wt.% IrO_2/C (light blue line), and carbon-supported amorphous iridium oxyhydroxide 30 wt.% $\text{a-IrO}_x(\text{OH})_y/\text{C}$ (red line). The arrows indicate the shift in binding energy of the peak maxima between the measured samples.

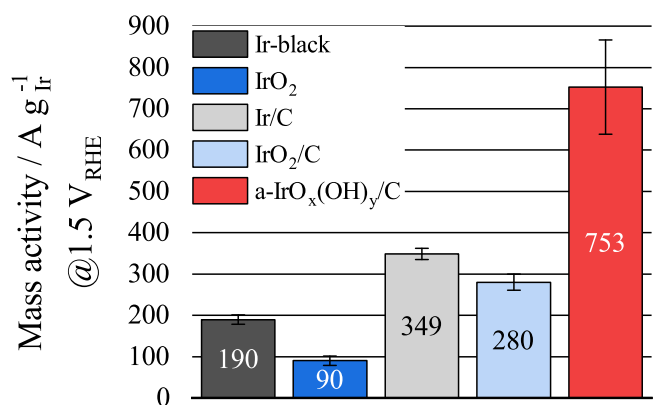


Figure 4. Mass activities towards the oxygen evolution reaction (OER) derived from RDE measurements (10 mV s^{-1} , 1600 rpm, 60°C , air sat. $0.5 \text{ M H}_2\text{SO}_4$) for the following OER co-catalysts: unsupported Ir-black (black), and IrO_2 (dark blue), carbon-supported metallic iridium 30 wt.% Ir/C (grey), carbon-supported crystalline iridium oxide 30 wt.% IrO_2/C (light blue), carbon-supported amorphous iridium oxyhydroxide 30 wt.% $\text{a-IrO}_x(\text{OH})_y/\text{C}$ (red). The error bars indicate the range between three individual measurements.

the nucleophilic attack of water or pre-adsorbed hydroxy groups.⁶⁴ In this context, a possible involvement of subsurface $\text{O}^{\text{I-}}$ species that migrate within the flexible $\text{Ir}^{\text{III/IV}}$ lattice to the surface and regenerate the active-sites under the OER potential has been postulated by Schlögl et al.⁷¹ Although in our work it was shown that the $\text{a-IrO}_x(\text{OH})_y/\text{C}$ possess a high Ir^{III} share (cf. Figs. 1b and 2e) and exhibits an outstanding OER activity (cf. Fig. 4, it would be of interest to consider “intrinsic” OER activities normalized to active-sites to finally support the high relevance of Ir^{III} moieties suggested by the authors. In this regard, one needs to determine the electrochemically active surface area of all OER co-catalysts employed to calculate surface specific OER activities. While it is rather well explored for metallic Ir catalysts from the charge of underpotentially deposited hydrogen (H_{upd})^{28,72} or the charge from CO electrooxidation in CO-stripping experiments,⁷³ different approaches have been controversially discussed and summarized⁷⁴ for IrO_2 , e.g. the most often applied method is using the double layer capacitance (C_{dl}). However, in case of supported catalysts, e.g. IrO_2/C or $\text{a-IrO}_x(\text{OH})_y/\text{C}$, complications imply due to the overlapping double layer capacitances from

the carbon support itself and the active species, which cannot be easily separated. Further, the amorphous iridium oxyhydroxide shows no features in the cyclic voltammogram in the low voltage regime (cf. Fig. 1b), which presumably indicates a vanishing catalyst film conductivity at low potentials³³ and impacts the double layer capacitance in the respective voltage regime. While the significance of determining intrinsic OER activities on a per active-site basis is acknowledged, particularly in relation to the chemical state of the investigated catalysts, we believe that pursuing such an analysis would require a more dedicated experimental design and data interpretation beyond the scope of the current study, especially if one consider determining the active-sites of the reactive Ir species at OER-relevant potentials $>1.4 V_{\text{RHE}}$.

With the awareness of the prevailing chemical state and catalytic activity on RDE-level, the OER co-catalysts were applied into PEM fuel cell anodes to enhance the stability against H_2 starvation. Figure 5 shows a representative plot of the cell voltage over time during the cell reversal experiments in single cell setup for MEAs containing Ir-black as an OER co-catalyst. The black solid line depicts the cell reversal data initially after break-in of the MEA, while the dotted line illustrates the data after seven days of continuous operation in H_2 . Figure S2 in the supplementary information provides the remaining materials in comparison. During the first 600 s the MEAs were conditioned as described in the experimental section. Thereafter, the H_2 starvation was triggered by feeding N_2 into the anode compartment while a current density of $0.2 \text{ A cm}^{-2}_{\text{geo}}$ was maintained, initiating a reversal of the cell voltage below 0 V with a subsequent plateau, often denoted as water electrolysis plateau.³⁹ By attaching a reference electrode and tracking the individual potentials of the anode and cathode, Taniguchi et al. determined that the sharp drop in cell voltage was related to an increase in the anode potential above $1.4 V_{\text{RHE}}$,⁷⁵ which is composed of the mixed potentials of the COR and OER taking place at the anode at different reaction rates. The time elapsed from the start of cell reversal until a cut-off voltage of -1.25 V is reached, is used as a measure of the cell reversal tolerance. Since the final cell reversal tolerance depends on the potential at which the cell voltage starts to plateau and how steep it declines, we applied a linear fit to the measured data within the range of 100 to 2000 s (grey area) to determine the onset voltage (y-axis intercept) and the voltage decay in mV h^{-1} (slope). The intersection of the measured data with -1.25 V (red dotted line) describes the cell reversal time. Both, the extracted onset voltages/slopes (Fig. 6) as well as the cell reversal time (Fig. 7) for the different OER co-catalysts are discussed in the following.

Figure 6 shows the slope over the onset voltage for the five MEAs comprising different co-catalysts. Full circles indicate the extracted data from cell reversal measurements initially taken after break-in of the MEAs, open circles after seven days of continuous operation in H_2 . The shaded rectangular clusters indicate the presumed predominant chemical state of the Ir co-catalysts, i.e. Ir^0 , Ir^{III} and Ir^{IV} . (A) Assessing the initial data set (full circles), the onset voltage increases in the order: Ir-black $\sim \text{IrO}_2 \ll \text{Ir/C} \sim \text{IrO}_2/\text{C} \ll \text{a-IrO}_x(\text{OH})_y/\text{C}$, which is in good agreement to the ranking of OER activities derived from RDE measurements. With the initiation of fuel starvation, several groups showed that the cathode potential remains nearly constant.^{45,49,75} Therefore, it is not surprising that the total cell voltage can be used to derive the activity of a co-catalyst towards the OER, i.e. the higher the OER activity, the lower the anode potential and the higher the onset of the total cell voltage. However, to get a more detailed understanding of a possible change in the structure and chemical state of the materials, the voltage decay could be used as a judging parameter. The steepness of slopes decreases in the following order: Ir-black $\sim \text{Ir/C} \ll \text{IrO}_2 \sim \text{IrO}_2/\text{C} \ll \text{a-IrO}_x(\text{OH})_y/\text{C}$, which leads to the assumption that the duration of the water electrolysis plateau is not only related to the activity of the OER catalyst but to the chemical and structural dynamical transformation of its predominant Ir-species at high anode

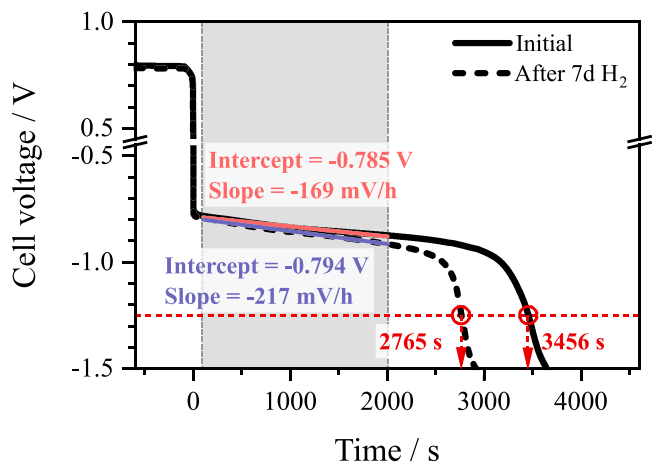


Figure 5. Representative cell voltage progression for membrane electrode assemblies (MEAs) containing Ir-black as oxygen evolution co-catalyst during cell reversal experiments, determined both initially after break-in of the MEAs (black solid line) and after seven days of continuous operation in H_2 (black dotted line). Grey area indicates the range for the linear fit. The intersection of the measured data with -1.25 V (red dotted line) describes the cell reversal time. Single cell setup, $0.2 \text{ A cm}^{-2}_{\text{geo}}$, 80°C cell temperature, RH of 100% for the supplied gases, $150/150 \text{ kPa}_{\text{abs,inlet}}$ total pressures and $1000/5000 \text{ nccm}$ constant flow rates for the anode and cathode, respectively.

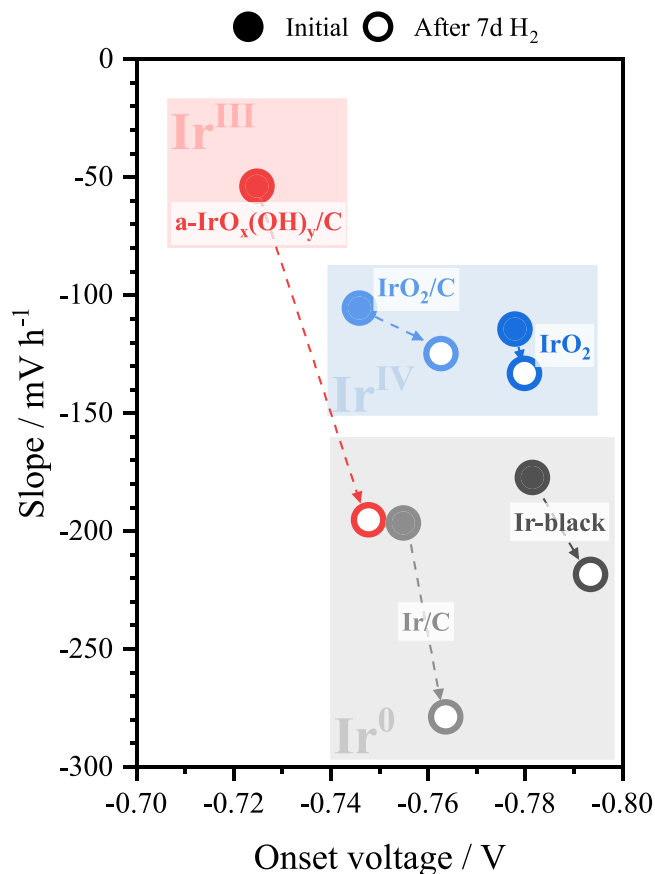


Figure 6. Employed oxygen evolution co-catalysts with the slope plotted over the onset voltage, derived from linear fit of cell voltage within the first 100–2000 s during cell reversal experiment (cf Fig. 5). Full circles: initially after break-in, open circles: after seven days of continuous operation in H_2 . The shaded rectangular clusters indicate the presumed predominant chemical state of the Ir co-catalysts, i.e. Ir^0 , Ir^{III} and Ir^{IV} .

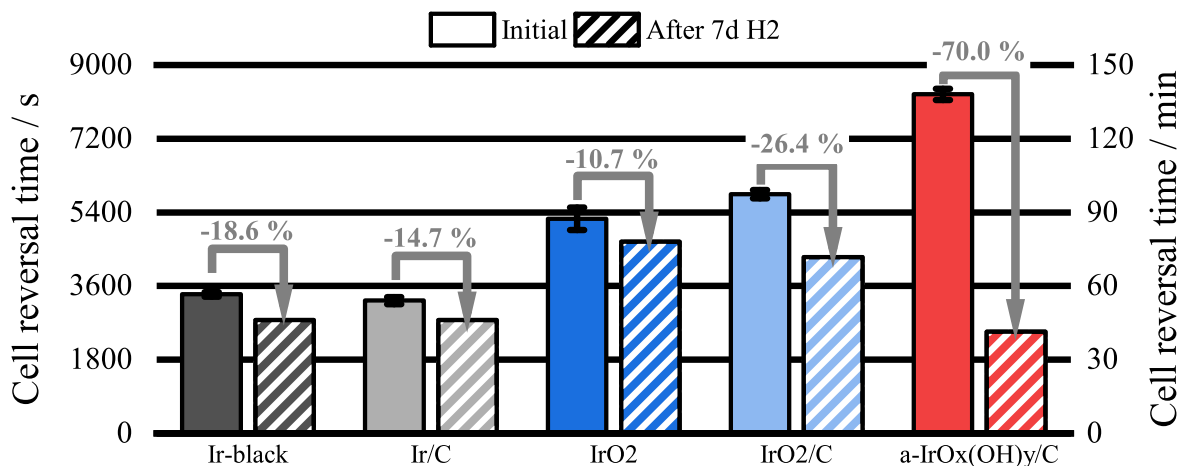


Figure 7. Bar chart showing the cell reversal time at -1.25 V for employed oxygen evolution co-catalysts determined both initially after break-in of the MEAs (solid bars) and after seven days of continuous operation in H_2 (striped bars). The error bars indicate the range between two individual measurements.

potentials. Indeed, it has been observed by others that metallic iridium, especially in the form of supported nanoparticles,²⁰ exhibit lower dissolution stability at high potentials compared to their oxidic form.^{27,35} We suggest that the stability of the OER co-catalyst is of importance for the stabilization of the water electrolysis plateau, which increasingly shifts toward carbon corrosion as the deactivation of the OER co-catalyst progresses. Although several different mechanisms for the failure of reversal-tolerant anodes have been described in the literature,^{38,76–78} the dissolution stability³⁵ of the predominant Ir-species has barely been considered to play a key role. (B) Examining the data set after seven days of continuous operation in H_2 (open circles), a distinct deterioration of the slope and onset voltage is evident for the anode comprising a- $IrO_x(OH)_y/C$, while the anode with IrO_2 shows the least change. As the supported amorphous iridium oxyhydroxide shows a similar slope to metallic iridium catalysts after prolonged operation under H_2 , it most likely can be concluded that it is reduced to Ir/C due to its rather easy reducibility. In contrast, the IrO_2 exhibits a low reducibility, which has been investigated by others as well by using ex-situ thermogravimetric analysis in forming gas on commercially available IrO_2/TiO_2 against IrO_2 (heat-treated at $500^\circ C$) and irreducible IrO_2 (highly heat-treated $650^\circ C$ – $1000^\circ C$).^{42,43} This observation suggests that rutile-type crystalline IrO_2 is an appropriate OER catalyst that largely retains its oxidation state, thereby ensuring sustained intrinsic stability of the anode catalyst layer during fuel starvation even after prolonged operation under H_2 atmosphere.

Figure 7 shows a bar chart comparing the cell reversal times at -1.25 V for the studied OER co-catalysts determined initially after break-in of the MEAs (solid bars) and after seven days of continuous operation in H_2 (striped bars). Strikingly, the initial tolerance for both the unsupported Ir-black and the supported metallic Iridium Ir/C is lowest at about 55 min, followed by the unsupported IrO_2 and supported IrO_2/C at 90 and 100 min respectively, and the highest measured tolerance for the supported a- $IrO_x(OH)_y/C$ with approx. 140 min. In contrast to the ranking of mass activities toward OER observed in the RDE measurements, there are only minor differences in cell reversal tolerance between the supported and unsupported Ir co-catalysts of a given chemical state, i.e. Ir^0 and Ir^{IV} . Although the metallic iridium co-catalysts show a somewhat higher OER activity in RDE compared to their crystalline oxide forms, high dissolution rates at high anode potentials^{27,35} appear to counteract due to deactivation of OER enhancing properties and thus diminishing cell reversal tolerances. Solely in the case of the a- $IrO_x(OH)_y/C$ with major Ir^{III} shares, high mass activity in the RDE correlates with high cell reversal stability. While the initial reversal tolerance directly after the break-in of the MEAs proceeds in the order Ir-black \sim Ir/C $<$ $IrO_2 \sim IrO_2/C <$ a- $IrO_x(OH)_y/C$, it changes drastically upon seven days of continuous operation under H_2 to a- $IrO_x(OH)_y/C \sim$

Ir-black \sim Ir/C $<$ $IrO_2/C \sim IrO_2$. In this context, the strongest decay of -70% in cell reversal tolerance is observed for the a- $IrO_x(OH)_y/C$, followed by a decay of -26% for the supported IrO_2/C , a minor drop of -14 to -18% for Ir/C and Ir-black, respectively, and the lowest change of -10% for IrO_2 , confirming a low reducibility under anode-relevant conditions for unsupported IrO_2 . Although, the Ir-black and Ir/C samples should not undergo any loss in cell reversal tolerance in the course of the seven-day operation under reductive conditions, they suffer from a non-negligible loss. While the relative loss in cell reversal tolerance for the metallic Ir-based catalysts appears to be somewhat higher than the loss for IrO_2 , the absolute loss lies in the same range of 400–630 s. We assume that this loss can be considered as baseline shift, attributed to morphological alterations and/or hydrophilicity changes^{79–81} of the electrode layer during prolonged operation, although an experimental evidence cannot be given in this study. Indeed, several studies suggest a rather sensitive dependency of the cell reversal tolerance on I/C ratio⁸² or water content^{15,76} variations in the electrode layer. On the other hand, the cell reversal tolerance of the a- $IrO_x(OH)_y/C$ co-catalyst decreased to the level of Ir-black and Ir/C, therefore we assume that it was almost completely reduced from Ir^{III} -rich oxidation state to metallic iridium (similar onset voltage and slope features, cf. Fig. 6) during the seven-day operation under H_2 atmosphere and $80^\circ C$. We suggest that Ir^{IV} -rich rutile-type IrO_2 is an appropriate OER co-catalyst that combines a decent OER activity with a good stabilization of its oxidation state Ir^{IV} , which means low chemical and structural changes at high anode potentials and high reduction stability at low anode potentials.

To provide additional insights on the prevailing change for the MEA containing a- $IrO_x(OH)_y/C$ (red colored), which has undergone the most severe decline in cell reversal tolerance, Fig. 8a shows the results of the CO-stripping experiment performed before the actual cell reversal test, directly after break-in (solid line) and after seven days of continuous operation in H_2 (dashed line). Notably, an additional experiment was conducted with a MEA without OER co-catalyst (Pt/C only, black colored) to separate the contribution of the OER co-catalyst to the CV features from that of the Pt/C. As expected, the largest contributor is the charge attributed to the CO electrooxidation at the Pt surface with a peak position at approx. $710 mV_{RHE}$ for all samples.⁸³ Instead of a dedicated CV feature, which could have been attributed to CO electrooxidation at a metallic Ir surface, only a minor underlying contribution for the samples comprising a- $IrO_x(OH)_y/C$ was found, which cannot be clearly attributed to CO electrooxidation on iridium but is in good agreement with the additional Ir-content in this MEA (Ir/Pt weight ratio 0.15). In this regard, a somewhat higher CO electrooxidation charge (10–14%) was observed for the MEA with a- $IrO_x(OH)_y/C$ (Initial: $139 C g_{Pt}^{-1}$, After 7d H_2 : $134 C g_{Pt}^{-1}$) compared to the

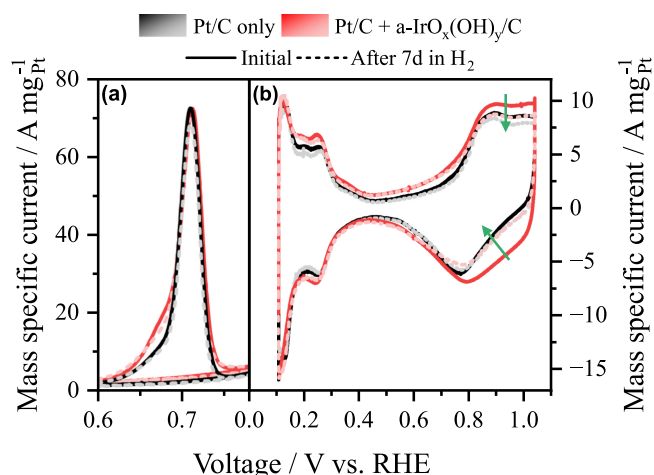


Figure 8. CO-stripping voltammograms (a) 1st and 2nd, (b) 3rd cycle of CV performed prior to cell reversal test. Pt/C only reference (black) and carbon-supported amorphous iridium oxyhydroxide 30 wt.% a- $\text{IrO}_x(\text{OH})_y/\text{C}$ (red) containing sample, initially after break-in of the MEAs (solid line) and after seven days of continuous operation in H_2 (dashed line). Single cell setup, 20 mV s^{-1} scan rate, 35°C cell temperature, RH of 100% for the supplied gases, ambient pressures and 50/500 nccm constant flow rates with $\text{N}_2/5\% \text{ H}_2$ (balance sat. N_2) for the anode and cathode, respectively.

Pt/C only reference (Initial: $122 \text{ C g}_{\text{Pt}}^{-1}$, After 7d H_2 : $113 \text{ C g}_{\text{Pt}}^{-1}$), indicating that near-surface metallic Ir may already be present for the samples after “short” break-in (8 h), previously being reported for $\text{IrO}_2/\text{TiO}_2$ catalysts.⁴² In this respect, no distinct difference in the CO electrooxidation charge was observed after extended operation in H_2 . However, in the subsequent CV in $\text{N}_2/5\% \text{ H}_2$ (balance sat. N_2) (Fig. 8b), significant differences were observed in the voltage range $>0.4 \text{ V}_{\text{RHE}}$ for the MEA with a- $\text{IrO}_x(\text{OH})_y/\text{C}$, while the Pt/C only sample shows only minor changes. The anode comprising amorphous Ir oxyhydroxide exhibits more pronounced redox features initially after break-in compared to the Pt/C only sample, which can be assigned to additional contributions originating from the transitions between Ir^{III} and Ir^{IV} , and vice versa (cf. CVs of OER catalysts in Fig. 1b), which also occur at least in part in the sub-surface structure of the OER additive. These redox features diminish after extended operation in H_2 , with the CV of the amorphous iridium oxyhydroxide almost completely following the Pt/C baseline, thus most likely indicating a (fully) reduced Ir additive after prolonged operation in H_2 .

Conclusions

The present study systematically investigated the cell reversal tolerance of PEM fuel cell anodes comprising different OER enhancing co-catalysts—unsupported and supported variants—which were initially analyzed by means of their prevailing chemical state, i.e. Ir^0 , Ir^{III} and/or Ir^{IV} . We found that the cell reversal tolerance is not solely dominated by the OER activity of the prevalent Ir-species but is likely related to its chemical and structural stability at high anode potentials, with oxidic iridium—both anhydrous and hydrated form—being more stable than metallic iridium. By performing cell reversal experiments immediately after break-in of the MEAs, we observed a superior cell reversal tolerance for the MEAs comprising Ir^{III} -rich a- $\text{IrO}_x(\text{OH})_y/\text{C}$, followed by the Ir^{IV} -rich IrO_2/C and IrO_2 , and metallic Ir/C and Ir-black placed lowest in the rankings. However, if the cell reversal experiment is preceded by prolonged operation under H_2 atmosphere, the ranking changes significantly, with the amorphous iridium oxyhydroxide showing a strongly diminished cell reversal tolerance in the order of metallic iridium co-catalysts, suggesting that it was reduced from Ir^{III} -rich to metallic Ir^0 . Since the chemical and structural properties of the co-catalysts appear to alter during operation under reductive conditions, we conclude that the cell reversal tolerances determined

immediately after break-in of the MEAs are less relevant for the real application than those after prolonged H_2 operation. Ultimately, IrO_2 provided a reasonable trade-off between initial OER activity, high structural and chemical stability at high anode potentials and high reduction stability under H_2 atmosphere, which resulted in a cell reversal time of approx. 90 min, which barely decreased when preceded by continuous H_2 operation. Rutile-type IrO_2 is an appropriate OER co-catalyst that combines a decent OER activity with a good stabilization of its oxidation state Ir^{IV} , thereby ensuring a sustained intrinsic cell reversal tolerance of the anode catalyst layer during hydrogen starvation even after prolonged operation under reductive atmosphere. Finally, this study emphasizes the importance of testing developed OER co-catalysts in application-relevant experiments to properly assess the suitability for the final application. This means simulating any occurring combination of operating conditions, such as low anode potentials during prolonged H_2 operation, high anode potentials during H_2 starvation events and/or transient potentials during start-up/shut-down events.

Acknowledgments

R.M., C.G. and F.E. gratefully acknowledge the Federal Ministry for Digital and Transport for financial support of this work within the DirectCCM project (NOW NIP II; Project No. 03B11011A). P.S. acknowledges financial support from the European Union’s Horizon Europe research and innovation programme under grant agreement BRAVA (Project No. 101101409) and HIGHLANDER (Project No. 101101346). The authors also thank all colleagues at Heraeus Deutschland GmbH & Co. KG, Global Business Unit Heraeus Precious Metals, Department Hydrogen Systems for many fruitful scientific discussions. Further, we thank Dieter Watzal from Heraeus’ internal analytics department for preparing and performing the XPS measurements.

ORCID

Robert Marić <https://orcid.org/0000-0003-4107-7461>
Peter Strasser <https://orcid.org/0000-0002-3884-436X>

References

1. D. A. Cullen, K. C. Neyerlin, R. K. Ahluwalia, R. Mukundan, K. L. More, R. L. Borup, A. Z. Weber, D. J. Myers, and A. Kusoglu, *Nat. Energy*, **6**, 462 (2021).
2. D. Y. Chung, J. M. Yoo, and Y.-E. Sung, *Advanced materials (Deerfield Beach, Fla.)*, **30**, e1704123 (2018).
3. D. Banham and S. Ye, *ACS Energy Lett.*, **2**, 629 (2017).
4. X. X. Wang, M. T. Swihart, and G. Wu, *Nat. Catal.*, **2**, 578 (2019).
5. I. C. Halalay, S. Swathirajan, B. Merzougui, M. P. Balogh, G. C. Garabedian, and M. K. Carpenter, *J. Electrochem. Soc.*, **158**, B313 (2011).
6. S. Henning, R. Shimizu, J. Herranz, L. Kühn, A. Eychmüller, M. Uchida, K. Kakinuma, and T. J. Schmidt, *J. Electrochem. Soc.*, **165**, F3001 (2018).
7. E. Hornberger et al., *ACS Catal.*, **8**, 9675 (2018).
8. T. Ioroi and K. Yasuda, *J. Power Sources*, **450**, 227656 (2020).
9. S. D. Knights, K. M. Colbow, J. St-Pierre, and D. P. Wilkinson, *J. Power Sources*, **127**, 127 (2004).
10. K. H. Lim, W. H. Lee, Y. Jeong, and H. Kim, *J. Electrochem. Soc.*, **164**, F1580 (2017).
11. H. Schmies et al., *Adv. Energy Mater.*, **8**, 1701663 (2018).
12. H. Schmies et al., *Chem. Mater.*, **30**, 7287 (2018).
13. C.-Y. Ahn et al., *Int. J. Hydrogen Energy*, **47**, 1863 (2022).
14. D.-H. Lee, G. Doo, S. Choi, D. W. Lee, J. Hyun, J. Kwen, J. Y. Kim, and H.-T. Kim, *J. Ind. Eng. Chem.*, **109**, 245 (2022).
15. B. K. Hong, P. Mandal, J.-G. Oh, and S. Litster, *J. Power Sources*, **328**, 280 (2016).
16. P. Mandal, B. K. Hong, J.-G. Oh, and S. Litster, *J. Power Sources*, **397**, 397 (2018).
17. T.-Y. Kim, S. W. Lee, and C. Pak, *J. Ind. Eng. Chem.*, **85**, 87 (2020).
18. F. Bizzotto, J. Quinson, A. Zana, J. J. K. Kirkensgaard, A. Dworzak, M. Oezaslan, and M. Arenz, *Catal. Sci. Technol.*, **9**, 6345 (2019).
19. C. Wang et al., *ChemSusChem*, **12**, 1576 (2019).
20. T. Reier, M. Oezaslan, and P. Strasser, *ACS Catal.*, **2**, 1765 (2012).
21. T. Reier, D. Teschner, T. Lunkenbein, A. Bergmann, S. Selve, R. Kraehnert, R. Schlögl, and P. Strasser, *J. Electrochem. Soc.*, **161**, F876 (2014).
22. D. Böhm, M. Beetz, C. Gebauer, M. Bernt, J. Schröter, F. Zoller, T. Bein, and D. Fattakhova-Rohlfing, *Applied Materials Today*, **24**, 101134 (2021).
23. M. Bernt, C. Schramm, J. Schröter, C. Gebauer, J. Byrnes, C. Eickes, and H. A. Gasteiger, *J. Electrochem. Soc.*, **168**, 84513 (2021).
24. M. Möckl, M. F. Ernst, M. Kornherr, F. Allebrod, M. Bernt, J. Byrnes, C. Eickes, C. Gebauer, A. Moskovtseva, and H. A. Gasteiger, *J. Electrochem. Soc.*, **169**, 64505 (2022).

25. C. Minke, M. Suermann, B. Bensmann, and R. Hanke-Rauschenbach, *Int. J. Hydrogen Energy*, **46**, 23581 (2021).
26. C. C. L. McCrory, S. Jung, I. M. Ferrer, S. M. Chatman, J. C. Peters, and T. F. Jaramillo, *JACS*, **137**, 4347 (2015).
27. S. Cherevko et al., *Catal. Today*, **262**, 170 (2016).
28. D. Rand and R. Woods, *J. Electroanal. Chem. Interfacial Electrochem.*, **55**, 375 (1974).
29. C. C. L. McCrory, S. Jung, J. C. Peters, and T. F. Jaramillo, *JACS*, **135**, 16977 (2013).
30. N. Danilovic et al., *J. Phys. Chem. Lett.*, **5**, 2474 (2014).
31. Y. Matsumoto and E. Sato, *Mater. Chem. Phys.*, **14**, 397 (1986).
32. G. C. Da Silva, N. Perini, and E. A. Ticianelli, *Appl. Catalysis B*, **218**, 287 (2017).
33. C. E. Moore, J. Eastcott, M. Cimentii, N. Kremliakova, and E. L. Gyenge, *J. Power Sources*, **417**, 53 (2019).
34. C. E. Moore, F. Afsahi, A. P. Young, and E. L. Gyenge, *J. Phys. Chem. C*, **123**, 23361 (2019).
35. S. Cherevko, T. Reier, A. R. Zeradjanin, Z. Pawolek, P. Strasser, and K. J. Mayrhofer, *Electrochem. Commun.*, **48**, 81 (2014).
36. M. Vuković, *J. Appl. Electrochem.*, **17**, 737 (1987).
37. J. Liao, S. Zaman, Y. Wang, M. Yang, L. Yang, M. Chen, and H. Wang, *ACS Appl. Mater. Interfaces*, **15**, 4092 (2023).
38. X. Zhou, Y. Yang, B. Li, and C. Zhang, *ACS Appl. Mater. Interfaces*, **13**, 2455 (2021).
39. C. Cai, Z. Wan, Y. Rao, W. Chen, J. Zhou, J. Tan, and M. Pan, *J. Power Sources*, **455**, 227952 (2020).
40. Y. Wang et al., *J. Power Sources*, **449**, 227542 (2020).
41. P. J. Rheinländer and J. Durst, *J. Electrochem. Soc.*, **168**, 24511 (2021).
42. M. Fathi Tovini, A. M. Damjanovic, H. A. El-Sayed, J. Speder, C. Eickes, J.-P. Suchsland, A. Ghielmi, and H. A. Gasteiger, *J. Electrochem. Soc.*, **168**, 64521 (2021).
43. M. Fathi Tovini, A. M. Damjanovic, H. A. El-Sayed, F. Friedrich, B. Strehle, J. Speder, A. Ghielmi, and H. A. Gasteiger, *Meet. Abstr.*, **MA2022-01**, 1466 (2022).
44. C. A. Reiser, L. Bregoli, T. W. Patterson, J. S. Yi, J. D. Yang, M. L. Perry, and T. D. Jarvi, *Electrochem. Solid-State Lett.*, **8**, A273 (2005).
45. R. Marić, C. Gebauer, M. Nesselberger, F. Hasché, and P. Strasser, *J. Electrochem. Soc.*, **167**, 124520 (2020).
46. M. Pourbaix, *Atlas of electrochemical equilibria in aqueous solutions* (National Assoc. of Corrosion Engineers, Houston, Tex) (1974).
47. R. Kötz, H. Neff, and S. Stucki, *J. Electrochem. Soc.*, **131**, 72 (1984).
48. S. J. Freakley, J. Ruiz-Esquius, and D. J. Morgan, *Surf. Interface Anal.*, **49**, 794 (2017).
49. L. Hu, B. K. Hong, J.-G. Oh, and S. Litster, *ECS Trans.*, **80**, 535 (2017).
50. P. Mandal, B. K. Hong, J.-G. Oh, and S. Litster, *ECS Trans.*, **69**, 443 (2015).
51. T. R. Ralph, S. Hudson, and D. P. Wilkinson, *ECS Trans.*, **1**, 67 (2006).
52. E. You, M. Min, S.-A. Jin, T. Kim, and C. Pak, *J. Electrochem. Soc.*, **165**, F3094 (2018).
53. S. Geiger, O. Kasian, B. R. Shrestha, A. M. Mingers, K. J. J. Mayrhofer, and S. Cherevko, *J. Electrochem. Soc.*, **163**, F3132 (2016).
54. V. Pfeifer et al., *Surf. Interface Anal.*, **48**, 261 (2016).
55. E. Özer, Z. Pawolek, S. Kühl, H. Nong, B. Paul, S. Selve, C. Spöri, C. Bernitzky, and P. Strasser, *Surfaces*, **1**, 151 (2018).
56. H.-S. Oh, H. N. Nong, T. Reier, A. Bergmann, M. Gliech, J. Ferreira de Araújo, E. Willinger, R. Schlögl, D. Teschner, and P. Strasser, *JACS*, **138**, 12552 (2016).
57. H. N. Nong et al., *Z. Phys. Chem.*, **234**, 787 (2020).
58. H. P. Tran, H. N. Nong, H.-S. Oh, M. Klingenhof, M. Kroschel, B. Paul, J. Hübner, D. Teschner, and P. Strasser, *Chem. Mater.*, **34**, 9350 (2022).
59. S. M. Alia and G. C. Anderson, *J. Electrochem. Soc.*, **166**, F282 (2019).
60. J. M. Campelo, D. Luna, R. Luque, J. M. Marinas, and A. A. Romero, *ChemSusChem*, **2**, 18 (2009).
61. M. Ledendecker et al., *Nano Res.*, **12**, 2275 (2019).
62. L. Ma, S. Sui, and Y. Zhai, *J. Power Sources*, **177**, 470 (2008).
63. S. Sui, L. Ma, and Y. Zhai, *Asia-Pacific J. Chem. Eng.*, **4**, 8 (2009).
64. V. Pfeifer et al., *Physical chemistry chemical physics: PCCP*, **18**, 2292 (2016).
65. V. Pfeifer et al., *Chem. Sci.*, **7**, 6791 (2016).
66. D. N. Buckley and L. D. Burke, *J. Chem. Soc., Faraday Trans. 1*, **71**, 1447 (1975).
67. M. Bernicke, E. Ortel, T. Reier, A. Bergmann, J. Ferreira de Araujo, P. Strasser, and R. Kraehnert, *ChemSusChem*, **8**, 1908 (2015).
68. H. N. Nong, H.-S. Oh, T. Reier, E. Willinger, M.-G. Willinger, V. Petkov, D. Teschner, and P. Strasser, *Angewandte Chemie (International ed. in English)*, **54**, 2975 (2015).
69. I. Jang, I. Hwang, and Y. Tak, *Electrochim. Acta*, **90**, 148 (2013).
70. A. Lončar, D. Escalera-López, S. Cherevko, and N. Hodnik, *Angew. Chem.*, **134**, e202114437 (2022).
71. C. Massué, V. Pfeifer, M. van Gastel, J. Noack, G. Algara-Siller, S. Cap, and R. Schlögl, *ChemSusChem*, **10**, 4786 (2017).
72. J. Mozota and B. E. Conway, *Electrochim. Acta*, **28**, 1 (1983).
73. J. Durst, C. Simon, F. Hasché, and H. A. Gasteiger, *J. Electrochem. Soc.*, **162**, F190 (2015).
74. M. D. Obradović, B. D. Balanč, U. Č. Lačnjevac, and S. L. Gojković, *J. Electroanal. Chem.*, **881**, 114944 (2021).
75. A. Taniguchi, T. Akita, K. Yasuda, and Y. Miyazaki, *J. Power Sources*, **130**, 42 (2004).
76. T. Joo, L. Hu, B. K. Hong, J.-G. Oh, and S. Litster, *J. Power Sources*, **472**, 228439 (2020).
77. Y. Wang et al., *Int. J. Hydrogen Energy*, **45**, 996 (2020).
78. C. Cai, Y. Rao, J. Zhou, L. Zhang, W. Chen, Z. Wan, J. Tan, and M. Pan, *J. Power Sources*, **473**, 228542 (2020).
79. J. Mitzel, Q. Zhang, P. Gazdzicki, and K. A. Friedrich, *J. Power Sources*, **488**, 229375 (2021).
80. X. Zhang, L. Guo, and H. Liu, *J. Power Sources*, **296**, 327 (2015).
81. Q. Zhang, M. Schulze, P. Gazdzicki, and K. A. Friedrich, *Appl. Energy*, **302**, 117490 (2021).
82. W. Chen, C. Cai, S. Li, J. Tan, and M. Pan, *Int. J. Hydrogen Energy*, **46**, 8749 (2021).
83. T. R. Garrick, T. E. Moylan, M. K. Carpenter, and A. Kongkanand, *J. Electrochem. Soc.*, **164**, F55 (2017).